Sensors & Actuators: B. Chemical 400 (2024) 134898

Contents lists available at ScienceDirect

Sensors and Actuators: B. Chemical

journal homepage: www.elsevier.com/locate/snb

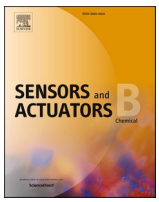

Towards cost-effective and lightweight surface plasmon resonance biosensing for H5N1 avian influenza virus detection: Integration of novel near-infrared organic photodetectors

Yu-Ching Huang [a,b,c,1], Sheng-Fan Wang [d,e,f,g,1], Bo-Cheng Chen [a], Zih-Syuan Yang [d,e], Meng-Chi Li [b,h], Xun-Ying Wu [i], Meng-Jey Youh [i,j], Hui-Yun Chou [i], Yu-Xen Lin [k], Wanchai Assavalapsakul [l], Arunee Thitithanyanont [m], Li-Chen Su [b,h,*]

[a] Department of Materials Engineering, Ming Chi University of Technology, New Taipei City 24301, Taiwan
[b] Organic Electronics Research Center, Ming Chi University of Technology, New Taipei City 24301, Taiwan
[c] Biochemical Technology R&D Center, Ming Chi University of Technology, New Taipei City 24301, Taiwan
[d] Center for Tropical Medicine and Infectious Disease Research, Kaohsiung Medical University, Kaohsiung 80708, Taiwan
[e] Department of Medical Laboratory Science and Biotechnology, Kaohsiung Medical University, Kaohsiung 80708, Taiwan
[f] Department of Medical Research, Kaohsiung Medical University Hospital, Kaohsiung 80708, Taiwan
[g] M.Sc. Program in Tropical Medicine, College of Medicine, Kaohsiung Medical University, Kaohsiung 80708, Taiwan
[h] General Education Center, Ming Chi University of Technology, New Taipei City 24301, Taiwan
[i] Department of Mechanical Engineering, Ming Chi University of Technology, New Taipei City 24301, Taiwan
[j] College of Engineering, Chang Gung University, Taoyuan 33302, Taiwan
[k] TeraOptics Corporation, Taoyuan, Taiwan
[l] Department of Microbiology, Faculty of Science, Chulalongkorn University, Bangkok, 10330, Thailand
[m] Department of Microbiology, Faculty of Science, Mahidol University, Bangkok 10400, Thailand

ARTICLE INFO

Keywords:
NIR SPR
Organic photodetector
3D printing
H5N1
AIV

ABSTRACT

H5N1 avian influenza virus (AIV) persists in causing highly fatal human infections, demanding rapid and accurate diagnostic assessment. In this study, we introduce an intensity-based SPR sensor utilizing NIR wavelength excitation in tandem with a specifically engineered NIR-OPD. The active layer of the OPD consists of a PTB7-Th and COTIC-4 F blend, offering an optimized response for a 980 nm excitation wavelength. Key performance metrics of this OPD include a low J_d of 0.185 nA/cm^2, a high responsivity of 0.35 A/W, an EQE of 44.74%, and an exceptional detectivity of 4.59×10^{13} Jones at 980 nm wavelength under zero bias. It also exhibits a wide LDR of 113 dB. The integration of such OPDs into our SPR sensor provides advantages in compactness and cost-effectiveness. Employing this sensor, we detected the H5N1 AIV using a custom high-affinity polyclonal antibody against HA envelope of the H5N1 virus, completing analyses of culture medium samples within 12 min. The detection limit of this biosensor for the H5N1 AIV in PBS-diluted culture medium is approximately 4.3×10^4 copies/mL. When compared to a commercial H5-Ag lateral flow test kit, our biosensor showed a sensitivity 37 times higher. Key attributes of our biosensor include 3D printing technology for easy alignment of optical components and a rapid, simplified detection procedure. Collectively, our findings open up the potential of our SPR biosensor as an efficient tool for detecting H5N1 AIV, promising advancements in on-site detection methodologies.

1. Introduction

Since 1997, highly pathogenic H5N1 avian influenza viruses (AIV) have caused numerous outbreaks in Southeast Asian chicken populations, leading to significant poultry deaths and depopulation [1,2]. These outbreaks occasionally result in H5N1 virus transmission to

* Correspondence to: General Education Center, Ming Chi University of Technology; Organic Electronics Research Center, Ming Chi University of Technology, New Taipei City 24301, Taiwan.
E-mail address: sulichen@o365.mcut.edu.tw (L.-C. Su).
[1] These authors equally contributed to this work.

https://doi.org/10.1016/j.snb.2023.134898
Received 16 August 2023; Received in revised form 30 October 2023; Accepted 1 November 2023
Available online 3 November 2023

humans, yielding a case fatality rate exceeding 50% [3]. Most recorded human cases have been linked to close contact with infected birds and contaminated environments. While sporadic and rare H5N1 virus infections in humans have been reported since December 2021, the World Health Organization (WHO) underscores the ongoing threat of H5N1 AIV to human health [4]. Urgent measures such as vaccine development, novel antiviral drugs, and prompt, accurate diagnostic assays with field-deployable capability are required to control and prevent this disease.

Surface Plasmon Resonance (SPR) biosensors have established their prominence in the field of molecular biology and biochemistry due to their ability to deliver real-time, label-free detection of biomolecular interactions [5–7]. These biosensors operate by utilizing the evanescent field, an electromagnetic field tightly bound to the metal-dielectric interface, which exponentially decays with distance. The evanescent field exhibits remarkable sensitivity to changes in the refractive index occurring on the sensor surface, allowing for the detection of minute variations resulting from biomolecular interactions. This exceptional sensitivity has positioned SPR biosensors as powerful tools in disease detection, diagnostics, drug discovery, and environmental monitoring. To further enhance the detection sensitivity of SPR sensors, researchers have been investigating the use of longer wavelength excitation [8–10]. This strategy capitalizes on the fact that longer wavelengths significantly enhance the evanescent field and increase its penetration depth [11–13]. By making slight adjustments to the incidence angle of a broadband light source, it becomes feasible to achieve longer wavelength excitation. This development holds great potential for improving the performance of SPR biosensors. The unique near-field optical characteristics of SPR biosensors, coupled with their highly sensitive detection capabilities that allow direct label-free detection of analytes, have bolstered their competitiveness in the portable and field-deployable biosensor [14–16].

Over the years, several practical SPR sensing techniques have been developed, including intensity interrogation, wavelength interrogation, angle interrogation, and phase interrogation. Each technique offers unique advantages and limitations, providing researchers with a range of options for SPR-based biosensing applications. In the angular interrogation mode, the incidence wavelength is fixed, and the shift of the SPR dip is monitored by continuously scanning the SPR angular graph [17–19]. This technique provides highly sensitive detection capabilities, allowing for precise monitoring of biomolecular interactions. However, angular interrogation suffers from certain drawbacks, such as the use of bulky and complex instrumentation, which limits its portability and practicality in some applications [20,21]. The wavelength interrogation mode, on the other hand, maintains a fixed angle of incidence while continuously obtaining the SPR spectral profile to monitor the SPR dip. This can be achieved by either scanning the incidence wavelength or using a spectrometer to analyze the reflected beam [22–24]. With the advent of miniaturized spectrometers, the wavelength-based SPR system has become more attractive as a portable and field-deployable biosensing platform compared to angle-based systems. While phase interrogation SPR techniques provide valuable insights into refractive index changes and offer potential sensitivity advantages in certain applications, they often necessitate the interference between a signal beam and a reference beam. This reliance on interference introduces complexity to the optics setup due to the inherent challenges associated with direct optical phase measurement [25–27]. In contrast, intensity interrogation SPR mode maintains a fixed incidence wavelength and angle, with the reflected light intensity directly monitored by a photodetector (PD) to quantify the refractive index variation of the sample [28–30]. This technique offers a simple structure design and does not require scanning or modulator devices, resulting in portability and cost-effectiveness [31].

In recent years, organic photodetectors (OPDs) have gained much attention due to their remarkable advantages, including tunability of detecting wavelength, high photocurrent, low-cost manufacture, compatibility with lightweight and flexible devices, and ease of processing [32–34]. These exceptional characteristics of OPDs have led to significant advancements in their performance and expanded their utility across a wide array of applications [35,36]. The enormous potential of OPDs has sparked intense research efforts. The focus is not only on understanding their unique properties but also on devising strategies to optimize their performance. A standout characteristic of OPDs is their ability to selectively detect different light ranges, including ultraviolet (UV), visible, and near-infrared (NIR) regions [37,38]. This versatility is facilitated by adjusting the optical bandgap of organic semiconductors and the strategic design of the device architecture of OPDs. For instance, incorporating narrow-bandgap non-fullerene acceptors (NFAs) can potentially extend the responsivity of OPDs into the NIR region [39–41]. Nonetheless, achieving high-performance NIR OPDs necessitates the effective suppression of dark current density (J_d). Recent research breakthroughs have been made in enhancing the performance of NIR-OPDs by reducing J_d including adjusting the thickness of the active layer, altering the energy bandgap of materials, and incorporating interfacial layers [42–44]. These improvements have paved the way for broader applications of OPDs, including biological imaging, sensing, optical communications, and night surveillance.

In this study, we present the development of an intensity-based SPR sensor that employs NIR wavelength excitation in combination with a specifically designed NIR-OPD. The featured NIR-OPDs use a narrow-bandgap NFA-based bulk heterojunction (BHJ), which incorporates a blend of PTB7-Th and COTIC-4 F to form the active layer. This design finely tuned the NIR response of the OPDs for an excitation wavelength of 980 nm. The fabricated OPD, with its active layer thickness carefully optimized, exhibits excellent performance parameters, including a low J_d of 0.185 nA/cm^2, high responsivity (R) of 0.35 A/W, impressive external quantum efficiency (EQE) of 44.74%, and an outstanding detectivity (D^*) of 4.59×10^{13} Jones at 980 nm wavelength under zero bias voltage. Moreover, it shows a broad linear dynamic range (LDR) of 113 dB. Incorporating such OPDs into our proposed intensity-based NIR SPR sensor paves the way for the development of compact and cost-effective optical detection units due to the superior responsivity and detectivity, even without an applied bias. As demonstrated by our experimental results, the refractive index sensitivity of our proposed sensor stands on par with other portable SPR sensors. To assess its bioapplicability, we employed this sensor for detecting the highly pathogenic H5N1 AIV by utilizing a custom-made high-affinity polyclonal antibody (pAb) against HA protein of the H5N1 virus. The fully optimized intensity-based NIR SPR biosensor demonstrated remarkable sensitivity and specificity towards the H5N1 virus, along with the ability to facilitate a rapid and straightforward analysis of culture medium samples within 12 min.

2. Materials and methods

2.1. Materials and NIR-OPDs fabrication

The structure of ITO/ZnO/PTB7-Th:COTIC-4 F/MoO_3/Ag was utilized to fabricate the NIR-OPD devices. We initiated the process by depositing ZnO as an electron transport layer (ETL) onto a cleaned ITO substrate, followed by a thermal treatment at 180 °C for 30 min. The synthesis of ZnO was accomplished through the sol–gel method, as detailed in our previous report [45]. PTB7-Th and COTIC-4 F were purchased from 1-Material Inc., and were dissolved at a weight ratio of 1:1.5 in O-xylene (20 mg/mL) with 2 vol% of 1-chloronaphthalene as an additive to form the active layer precursor. The active layer was deposited onto the ZnO-coated substrate inside a glove box by spin-coating. By varying the spin-coating rate, we obtained active layers with distinct thicknesses, specifically 88 nm, 92 nm, 104 nm, and 150 nm. Subsequently, MoO_3 (5 nm) and Ag (100 nm) were deposited onto the active layer through thermal evaporation to serve as a hole transport layer (HTL) and top electrode, respectively. The resulting NIR-OPD

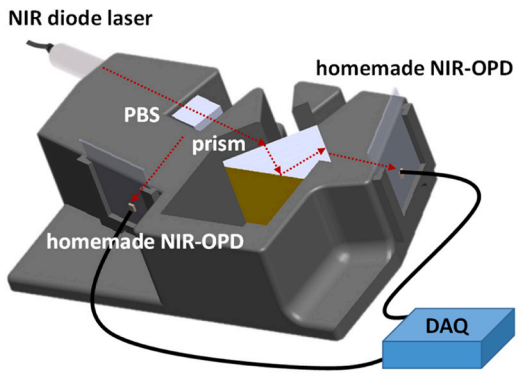

Fig. 1. Schematic representation of the intensity-based NIR SPR biosensor. The platform integrates an NIR light source, NIR-OPDs, a DAQ, and a custom-made 3D-printed SPR module, outfitted with a polarizing beamsplitter (PBS) and prism.

device area was 0.04 cm^2.

2.2. NIR-OPDs characterization

The thickness of the film was assessed using an Alpha-stepper from Bruker. The dark current density-voltage (J_d–V) and noise current characteristics of the devices were recorded using a source meter from Keithley 2636. The EQE spectra and responsivities ranging from 300 to 1200 nm were measured under zero bias voltage. This measurement was taken using a QE-R system from Enlitech (Kaohsiung, Taiwan) and a silicon-based photodetector (model: S1337) provided by Hamamatsu. The photocurrent variation to light intensity was evaluated by scrutinizing the LDR. In order to quantify the LDR, a laser diode emitting at 980 nm (CPS980, Thorlabs) was directed at a motorized filter wheel (FW102CNEB, Thorlabs) to create a controlled light intensity over the area of the OPD device.

2.3. Simulation of SPR Curve for the NIR light source

In our methodology, a significant step was conducting a rigorous simulation to depict the SPR curve of reflectance versus angle of incidence, particularly optimized for a 980 nm light source. Utilizing the Essential Macleod simulation software, renowned for modeling and analyzing optical thin film coatings, we modeled the sensor's thin film layers with the refractive indices of Au and Cr, denoted as 0.19 + 3.59i and 4.25 + 4.72i, respectively, at the wavelength of 980 nm [46,47]. The simulation was conducted in an environment of phosphate-buffered saline (PBS), with a refractive index of 1.3344. Our focus was on identifying the incident angle at which the SPR curve exhibited the steepest slope, indicative of maximal sensitivity to refractive index variations. This simulation laid the foundational groundwork that informed the subsequent experimental designs and analyses featured.

2.4. Design of the intensity-based NIR SPR biosensor

Our purposefully designed NIR SPR biosensor was built with an intensity interrogation approach using custom-made 3D-printed components. The sensor was designed to utilize the 980 nm NIR laser, which is routed through a polarizing beamsplitter, dividing it into an s-polarized reference beam and a p-polarized detection beam. The p-polarized beam was then directed onto the sensor surface through a prism at a predetermined angle. The 3D-printed SPR module with the optimal angle which was carefully designed and identified by an experiment using a rotation stage on an optical table. Then, the specially designed NIR-OPD, which operates without an external applied bias, was integrated into the 3D-printed SPR module to collect the light reflected from the sensor surface. Meanwhile, another NIR-OPD monitors any fluctuations in the s-polarized reference beam to account for any changes in the light source intensity. A DAQ device is employed to facilitate simultaneous recording

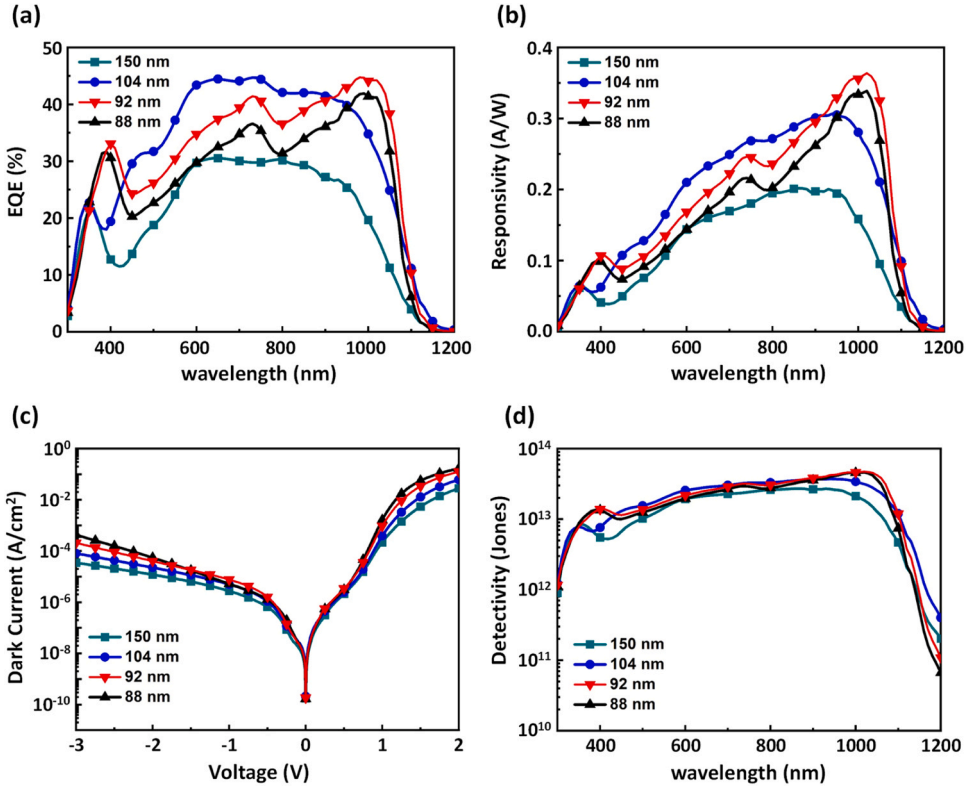

Fig. 2. Comprehensive characterization of the homemade NIR-OPDs featuring varied thicknesses in the active layer. (a) EQE spectra, (b) device responsivities, and (c) dark current densities (d) shot-noise-limited specific detectivities.

Table 1
Performance characteristics of OPDs fabricated with distinct active layer thicknesses measured at 0 V Bias.

Activity layer thickness (nm)	EQE (%) @ 980 nm	R (AW^{-1}) @ 980 nm	J_d (A / cm^2)	D* (Jones) @ 980 nm	LDR (dB) @ 980 nm
88	**41.77**	**0.33**	**1.68×10^{-10}**	**4.49×10^{13}**	**112**
92	**44.74**	**0.35**	**1.85×10^{-10}**	**4.59×10^{13}**	**113**
104	**37.58**	**0.29**	**2.11×10^{-10}**	**3.61×10^{13}**	**104**
150	**22.26**	**0.17**	**1.73×10^{-10}**	**2.36×10^{13}**	**97**

of signals from both NIR-OPDs. Fig. 1 provides a schematic representation of the optical setup for our intensity-based NIR SPR biosensor. The assembled device has a compact footprint of 12 × 7 cm and it's 2.5 cm tall.

2.5. Fabrication of the 3D-printed SPR module

The design of the SPR module was conceived using SolidWorks software, with the physical construction accomplished using a CREALITY 3D printer (model: CR-6 SE, Shenzhen, China). Following the design phase, slicing was executed employing an Ultimaker Cura, under the prescribed parameters: layer height set to 0.2 mm, 5 perimeters, an infill of 25%, a printing temperature maintained at 200 °C, a print bed temperature of 60 °C, a print speed of 50 mm/s, and a fan speed at full capacity (100%). To secure appropriate adhesion, the print bed was coated with a layer of polyvinylpyrrolidone glue. The material employed for the fabrication process was a solid polymer wire made of polylactic acid. Once the 3D-printed SPR sensor construction was completed, the challenges in optical alignment of non-visible light was elegantly addressed, all the while maintaining a compact form factor.

2.6. Preparation of SPR bio-sensing surface

In this study, we employed carboxymethyl-dextran CM3 chips (Cytiva). These chips possess shorter dextran chains compared to CM5 and are recommended for the analysis of larger molecules relative to CM5 sensor chips [48]. We immobilized the capture antibody, anti-H5 pAb, specific to the H5N1 virus, onto these chips using a Biacore T200 instrument (Cytiva). The immobilization achieved a level of 3000 RU, corresponding to an approximate refractive index change of 3×10^{-3} RIU [49]. To modify the surface of the SPR chips, we employed the standard amine coupling procedure, which has been extensively outlined in prior literature [24,27,50]. The anti-H5 pAb, prepared as per the methods detailed in previous research, has been proven to specifically recognize HA proteins of the A/Vietnam/1203/04 (H5N1) reverse-genetics (RG) strain [51]. Upon completion of these procedures, the SPR chips were primed and ready for integration into our proposed biosensor.

3. Results and discussion

3.1. Performance Characterization of NIR-OPD and optimization of the active layer thickness

Our group has previously demonstrated a BHJ blend, which incorporates a blend of PTB7-Th and COTIC-4 F to form a charge generation layer (CGL) [52]. A notable feature of this design is its ability to extend the absorption spectrum into the NIR region, achieving spectral coverage on par with conventional silicon photodiodes. This development has profound implications for subsequent applications of the NIR-OPD. In this section, we focus on refining the active layer thickness of the OPD to optimize its performance characteristics under the 980 nm wavelength light source deployed by our proposed NIR SPR biosensor.

We examined active layers fabricated from PTB7-Th:COTIC-4 F, specifically those with thicknesses of 88 nm, 92 nm, 104 nm, and 150 nm. The corresponding EQE spectra of these OPDs under 0 V bias are depicted in Fig. 2a. Notably, at a wavelength of 980 nm, the EQE performance sees a boost the active layer thickness increasing from 88 nm to 92 nm. However, further thickening the active layer results in a decreasing EQE, which may be attributed to the low charge mobility of organic semiconductors leading to an increase in recombination loss in the thick film [35,53]. A peak EQE of 44.74% is achieved with an active layer thickness of 92 nm, marking a twofold improvement over the OPD with a 150 nm thick active layer. The responsivity of the devices was derived using Eq. (1).

$$R(\lambda) = \mathrm{EQE}(\lambda) \times \frac{q\lambda}{h\nu} \tag{1}$$

with q representing the fundamental charge (1.602×10^{-19} C), λ indicating the incident wavelength, h referring to Planck's constant, and ν standing for the frequency of the light source. The resultant responsivity values are displayed in Fig. 2b and Table 1. The responsivities of devices fabricated with active layer thicknesses of 88 nm, 92 nm, 104 nm, and 150 nm, at a wavelength of 980 nm, were 0.33, 0.35, 0.29, and 0.17 A/W, respectively. Fig. 2c uncovers the influence of active layer thickness on the J_d. At 0 V bias, all devices exhibited similar and exceedingly low values of J_d, with the lowest J_d of 0.185 nA/cm^2 achieved with a 92 nm thick active layer. In summary, the NIR-OPD outfitted with a 92 nm thick active layer showed the maximum detectivity of 4.59×10^{13} Jones at a wavelength of 980 nm (refer to Fig. 2d and Table 1). The shot-noise-limited specific detectivity (D^*) was determined from Eq. (2).

$$D^* = \frac{R}{\sqrt{2qJ_d}} \tag{2}$$

The evaluation of the total noise current is crucial, as it is largely comprised of thermal noise, shot noise, and flicker noise. This step ensures that the shot-noise-limited D^* is not overestimated. Fig. S1a presents the noise currents of the devices at 0 V, and Fig. S1b displays the actual D^* values in relation to the noise current. The peak D^* at a 980 nm wavelength also occurs in the 92 nm thick active layer (Table S1), consistent with results obtained when considering only the shot-noise-based sample. After considering both the response and device performance at a 980 nm wavelength, we concluded that the optimal thickness for the active layer in our NIR-OPDs is 92 nm. Subsequently, we investigated another crucial OPD metric, the LDR, which represents the operational light intensity range of the device. LDR was calculated using Eq. (3).

$$LDR = 20\log\left(\frac{J_{\max}}{J_{\min}}\right) \tag{3}$$

where $J_{\max}$ denotes the current density at the highest light intensity, while $J_{\min}$ represents the current density at the lowest light intensity, with linearity maintained. Table 1 and Fig. S2 provide an overview of the LDRs of the OPDs tested with a 980 nm light source under 0 V bias. At 980 nm, the LDRs of the devices fabricated with active layer thicknesses of 88 nm, 92 nm, 104 nm, and 150 nm were 112 dB, 113 dB, 104 dB, and 97 dB, respectively. The wide range of LDRs suggests this device's capacity to efficiently detect light intensity under low-light conditions. A wide LDR, coupled with high D^*, at a 980 nm wavelength, signifies that a 92 nm thick active layer could be a suitable candidate for integration into the proposed NIR SPR biosensor. Consequently, in the subsequent SPR experiments, we utilized the NIR-OPD consisting of PTB7-Th:COTIC-4 F with an active layer thickness of 92 nm.

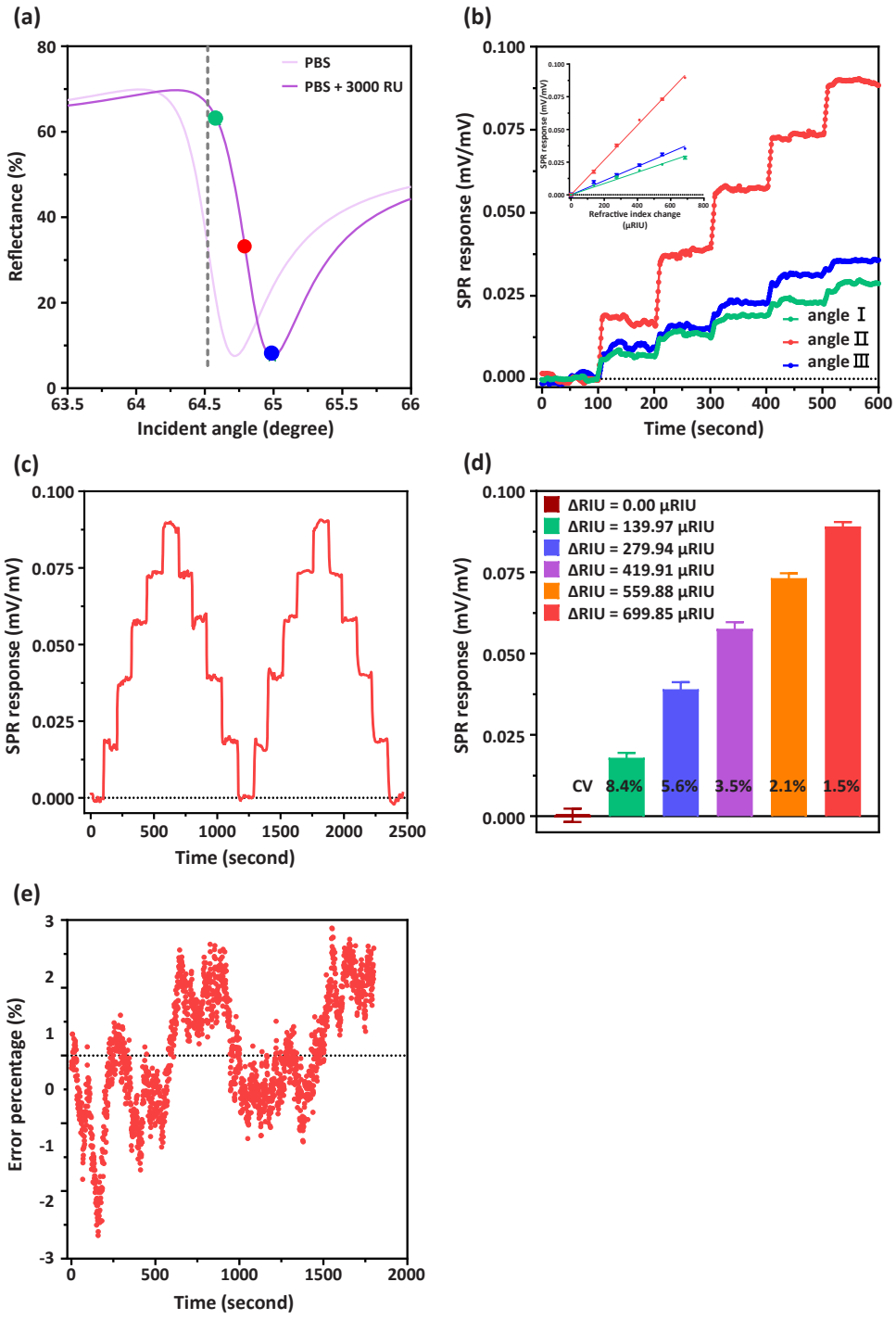

Fig. 3. Evaluation of the detection performance for the proposed NIR SPR biosensor. (a) The simulation results of the SPR curve of reflectance versus incident angle for 980 nm light source corresponding to environmental refractive indices of 1.3344 (representative of phosphate-buffered saline (PBS), the light purple SPR curve) and 1.3374 (representative of the immobilization of capture Ab for 3000 RU approximately, the purple SPR curve). (b) The SPR responses with respect to time and concentration at the three incident angles. Inset is the relationship between the SPR responses and the refractive index change for the three incident angles. (c) Repeatability response curve of the proposed NIR SPR biosensor to refractive index changes at the optimal incident angle. (d) A bar graph depicting the CV for each concentration level during the two cycles. (e) The system stability of the 3D-printed SPR module over a period of 30 min.

3.2. Optical Characterization of the intensity-based NIR SPR biosensor

In the case of the intensity-based SPR sensor, it operates at a fixed incident angle, measuring directly from the intensity of the reflected light. However, the SPR angle that possesses the minimum reflected light intensity does not necessarily coincide with the optimal incident angle of the light source for the intensity-based SPR sensing technique. This is due to the fact that at this incident angle, i.e. SPR angle, the slope of the SPR curve of reflectance versus incident angle is not the steepest, suggesting that the change in reflected light intensity with the refractive index is not acutest. Therefore, we sought to find the steepest slope of the SPR curve under 980 nm light source, which would then be used as the incident angle for our 3D-printed SPR module.

The simulation results reveal that the minimum reflection point (dip)

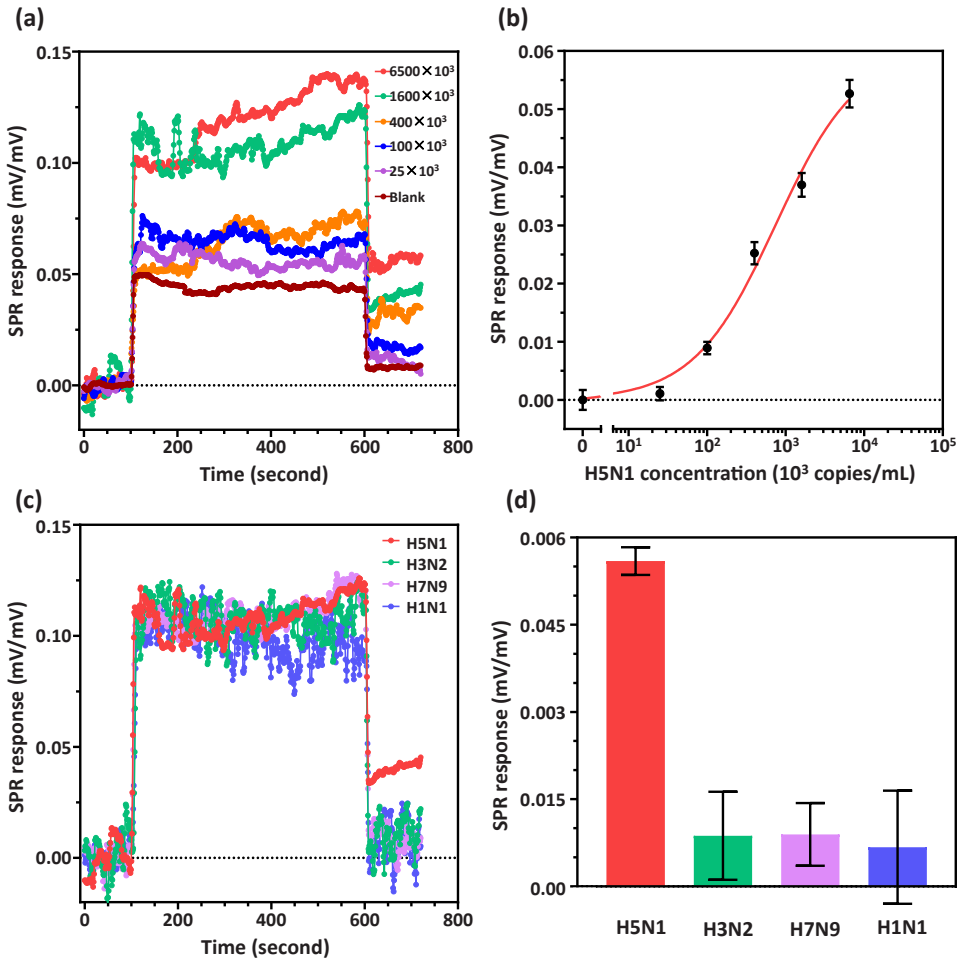

Fig. 4. Assessment of the bio-applicability for the proposed NIR SPR biosensor by H5N1 AIV detection. (a) SPR sensorgrams corresponding to diverse H5N1 AIV concentrations. (b) Standard curve representation for H5N1 AIV ranging from 2.5×10^4 to 6.5×10^6. (c) SPR sensorgrams for the specificity tests. (d) SPR responses for samples inclusive of H5N1 AIV compared to non-specific samples (H3N2, H7N9, H1N1).

of the SPR curve is situated at incident angles of 64.7° and 65.0°, corresponding to environmental refractive indices of 1.3344 (representative of PBS, the light purple SPR curve in Fig. 3a) and 1.3374 (representative of the immobilization of capture Ab for 3000 RU approximately, the purple SPR curve in Fig. 3a). According to the simulation results, it is apparent that if the incident angle of the light source is fixed at the optimum angle (gray dash line in Fig. 3a) for PBS, the angle exceeds the measurement range subsequent to the capture Ab modification, rendering biological experiments impossible. This limitation stems from the face that while the SPR sensing platform developed with NIR light sources is more sensitive to refractive index changes than systems constructed with red light, it has a smaller detection range. This is due to the narrower full width at half maximum (FWHM) of the SPR curve and the larger curve shift for the same refractive index changes when NIR is used as the light source in comparison to red light. Thus, in this study, the light source incident angle of our 3D-printed SPR module was selected based on the optimum incident angle derived from the simulation of the CM3 chip modified with 3000 RU of anti-H5 pAb.

Next, we utilized a rotation stage on an optical table to identify the incident angle that resulted in the minimum reflection for the CM3 chip, which was modified with 3000 RU of anti-H5 pAb. Subsequently, we conducted experiments to evaluate the physical sensitivity to changes in the refractive index at three specific incident angles: the SPR angle, SPR angle - 0.2°, and SPR angle - 0.4°, which correspond to the blue dot, red dot, and green dot in Fig. 3a, respectively. We employed analytes in the form of PBS-diluted glycerin solutions to induce a refractive index change from 1.3997×10^{-4} RIU to 6.9985×10^{-4} RIU, which the values were confirmed using the Biacore T200 instrument. Upon the respective solutions being injected into the reaction chamber, SPR responses which were obtained by dividing the signal of the reflected light to that of the s-polarized reference beam to reduce the disturbances that arise from light source noise [29,54], were recorded and presented in Fig. 3b. The SPR responses of three incident angles increased with the refractive index change, as shown in Fig. 3b. The inset in Fig. 3b depicts the linear relationship between refractive index changes and SPR responses for the three incident angles. The slopes of the linear fitting curves represent the sensitivity to detecting refractive index changes and were estimated to be 17250/RIU, 53285/RIU, and 21679/RIU for the three incident angles of SPR angle, SPR angle - 0.2°, and SPR angle - 0.4°, respectively. Furthermore, the error bars represent one standard deviation in each measurement. The results in Fig. 3b demonstrate that the incident angle with SPR angle - 0.2° has a higher sensitivity in detecting refractive index changes than the other two incident angles, and the corresponding physical detection limit was estimated to be around 10^{-6} RIU. Moreover, the coefficients of variation (CV) of the proposed biosensors are between 1.5% and 8.4%, demonstrating good reproducibility, as shown in Fig. 3c and d. On the other hand, based on the theoretical simulations under our experimental conditions, the incident angles between SPR angle - 0.15° and SPR angle - 0.2° showed the highest sensitivity to refractive index changes and the values were very close. Thus, considering the fabrication tolerance of our SPR module design, we ultimately selected SPR angle - 0.2° as the incident

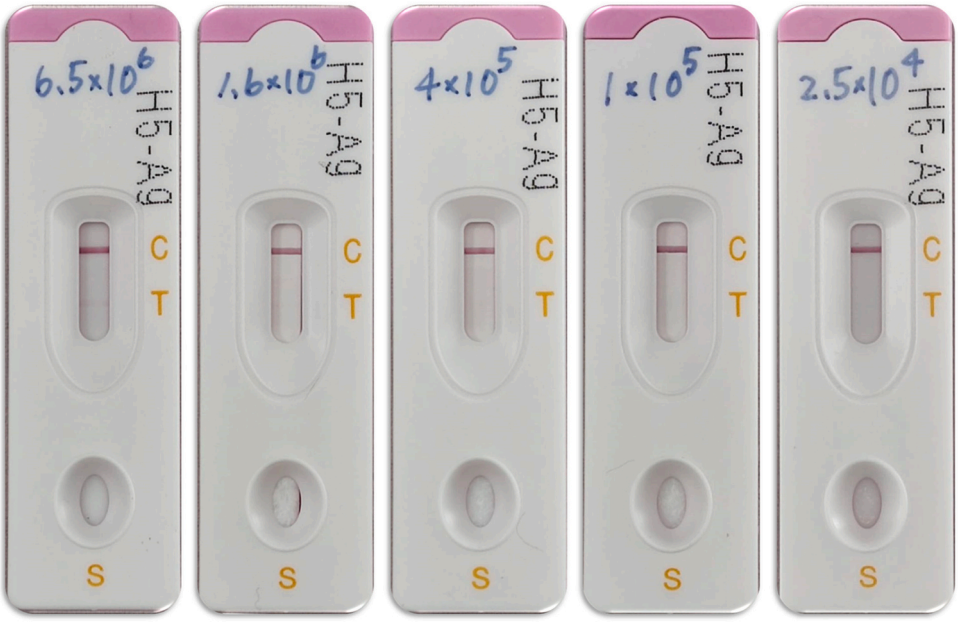

Fig. 5. Results obtained using commercial H5-Ag lateral flow test kits.

angle to construct the 3D-printed SPR module used in the following experiments.

After fabricating the 3D-printed SPR module, we measured the system stability, which was expressed as the system's percentage error. This error was calculated by $\frac{A_{each\ point}-A_{mean}}{A_{mean}}$, where "A" was the SPR response. As shown in Fig. 3e, the standard deviation of system stability is 1% over a period of 30 min. It's important to note that the detection performance of SPR biosensors is predominantly determined by system stability, which considerably depends on the light source stability and detector noise level [55]. In the past, we established a bench-top intensity-based SPR system, which adopted a balance detection technique to improve the signal-to-noise ratio, thereby achieving high detection performance [29]. For this study, we employed a cost-effective 980 nm diode laser as the light source, and the intensity signal was obtained using a home-made OPD device. Combined with our custom-made 3D-printed SPR module, these components were seamlessly integrated to form an efficient, cost-effective, compact, and controllable SPR measurement system, which demonstrated a stability performance close to that in the past study.

3.3. Detection of H5N1 Avian influenza virus

To assess the applicability of our proposed intensity-based NIR SPR biosensor for biomedical detection, we conducted experiments with the H5N1 AIV in culture medium. The ongoing epizootic of highly pathogenic avian influenza caused by H5N1 in poultry exhibits an unprecedented level of virulence, extent, and duration. This phenomenon has raised global apprehension due to the potential for the virus to undergo mutations facilitating human-to-human transmission, thereby instigating an H5N1 influenza pandemic [56]. The expeditious and precise execution of diagnostic assays with field-deployable capability is of paramount importance to mitigate the morbidity and mortality associated with H5N1-infected poultry and to curtail the pandemic potential. Nevertheless, the majority of commercially available kits and rapid tests exhibit inherent limitations in detection sensitivity for H5N1 avian influenza in veterinary applications [57]. This underscores the pressing need for an easy-to-use and sensitive detection platform that enables farm workers to effortlessly conduct the tests for the H5N1 AIV accurately. Given its attributes such as label-free and real-time measurement capabilities combined with high sensitivity, the SPR technique indeed emerges as a promising contender in this scenario.

In this study, we evaluated the initial titer of H5N1 AIV in culture medium as 2.6×10^7 copies/mL through qRT-PCR and utilized PBS to perform a four-fold dilution of this virus-laden culture medium (noted as d-4 VM). We prepared a four-fold PBS dilution of blank culture medium (noted as d-4 BM) and utilized this dilution to further dilute d-4 VM to 6.5×10^6, 1.6×10^6, 4.0×10^5, 1.0×10^5, and 2.5×10^4 copies/mL. These dilutions were individually injected into the reaction chamber and their resulting sensograms were observed. The time-dependent changes in intensity resulting from the binding of the H5N1 AIV to the anti-H5 antibody immobilized on the chip are shown in Fig. 4a. We observed that as the concentration of the H5N1 AIV increased, so did the SPR response, with the total testing time controlled within 12 min for each instance. The relationship between the SPR response and the concentration of the H5N1 AIV, within the range of 2.5×10^4 copies/mL to 6.5×10^6 copies/mL, is shown in Fig. 4b, with results analyzed using four-parameter logistic regression. Based on the definition by IUPAC, the detection limit of the proposed intensity-based NIR SPR biosensor for detecting H5N1 AIV in PBS-diluted culture medium is estimated to be 4.3×10^4 copies/mL.

Additionally, the specificity of the proposed detection platform, or more precisely, the antibodies employed in this study, for the H5N1 AIV was evaluated. This assessment involved four strains of Influenza A viruses, including three AIVs (H3N2, H5N1, and H7N9) and seasonal H1N1 influenza virus. In these experiments, the concentration of the three test viruses and the H5N1 AIV was 6.5×10^6 copies/mL and 1.6×10^6 copies/mL, respectively, both in four-fold PBS-diluted culture medium. The sensograms of the three test viruses and the H5N1 AIV are depicted in Fig. 4c. It is apparent that the SPR responses, before sample injection and after washing, of the three test viruses are significantly lower than that of the H5N1 AIV as displayed in Fig. 4d. This indicates that the three test influenza viruses were not detected by the proposed method. Taken together, these results demonstrate that, with highly specific antibodies, the proposed platform indeed exhibits high specificity in detecting the H5N1 AIV.

Finally, we compared the detection performance of our proposed intensity-based NIR SPR biosensor with a commercial H5-Ag lateral flow test kit (Elabscience Biotechnology Inc., Houston, Texas) available in the market. The results in Fig. 5 show that the detectable concentration of the commercial kit is approximately 1.6×10^6 copies/mL, which is 37

Table 2
Method comparison for AIV detection.

Detection technique	Portability	Assay time	Target	LOD	Ref.
Single-nanoparticle Collision Electrochemistry	**x**	**5.5 hr**	**H7N9**	**24.3 fg/mL**	[58]
Functional Silica Nanospheres, MBs, Electrochemiluminescence	**x**	**1 hr**	**H9N2**	**14 fg/mL**	[59]
Electrochemical Impedance Spectroscopy	**x**	**45 min**	**H9N2**	**6.7 pfu/50 μL**	[60]
Self-calibrating Electrochemical Aptasensing	**x**	**30 min**	**nucleoprotein**	**$10^{4.865}$ EID_{50}/mL**	[61]
Self-calibrating Luminescence Resonance Energy Transfer	**x**	**10 min**	**nucleoprotein**	**0.38 pM**	[62]
Extended-gate FET	**v**	**2 hr**	**H5N1 HA protein**	**5.9 pM**	[63]
Fluorescence Polarization Immunoassay	**v**	**20 min**	**anti-H5 antibody**	**20-fold dilution**	[64]
Catalytic Hairpin Assembly, G-quadruplex Fuorescence Probe	**v**	**20 min**	**H5N1**	**129 pM**	[65]
Chemiluminescent Lateral Flow	**v**	**15 min**	**nucleoprotein**	**$10^{4-2.5}$ EID_{50}/mL**	[66]
SPR with NIR OPD	**v**	**12 min**	**H5N1**	**4.3×10^4 copies/mL**	**This study**

times less sensitive than the LOD of the proposed SPR biosensor, estimated at around 4.3×10^4 copies/mL. We have also summarized the performance comparison of various detection methods and the proposed intensity-based NIR SPR biosensor, focusing on sensitivity, portability, and assay time, in Table 2 [58–66]. It's worth emphasizing that this comprehensive evaluation distinctly underscores the resilience and competitive advantage of our SPR integrated with NIR OPD biosensor amidst a diverse range of existing methodologies. Current strategies to prevent the H5N1 AIV rely primarily on regular testing of sick poultry on farms to break the chain of transmission and infection. Therefore, we believe that the proposed SPR biosensor, integrated with highly specific antibodies, holds significant potential to serve as an effective detection platform for the H5N1 AIV.

4. Conclusions

In this study, we have successfully integrated a self-fabricated organic photodetector and 3D printing technology to develop an intensity-based NIR SPR biosensor. Its physical performance and biomedical applicability have been thoroughly validated. The distinguishing features of this biosensor are: (1) owing to the superior refractive index sensitivity of SPR biosensors in the NIR range compared to the visible range, and the relatively simple optical setup required for intensity-based SPR that merely necessitates the monitoring of reflected light intensity by a photodetector. (2) We designed and fabricated an organic photodetector specific to the 980 nm wavelength light source employed in our system. We also determined the optimal thickness of the active layer to maximize detection performance. (3) The utilization of 3D printing technology renders the alignment of optical components straightforward, overcoming the challenges of optical alignment in the NIR range (non-visible light), while maintaining a compact form factor and lightweight design. (4) Our proposed platform has successfully detected the H5N1 AIV in cell culture fluid samples, with detection completed using a simplified analysis procedure in less than 12 min. In conclusion, our research presents a facile SPR biosensing platform for the detection of highly pathogenic viruses. We optimistically anticipate that this platform will open new avenues in the field of on-site detection.

CRediT authorship contribution statement

Yu-Ching Huang: Conceptualization, Methodology, Investigation, Writing – review & editing, Funding acquisition. **Sheng-Fan Wang:** Conceptualization, Methodology, Investigation, Writing – review & editing, Funding acquisition. **Bo-Cheng Chen:** Validation, Investigation. **Zih-Syuan Yang:** Validation, Investigation. **Meng-Chi Li:** Investigation, Software. **Xun-Ying Wu:** Investigation, Data curation. **Meng-Jey Youh:** Methodology, Resources. **Hui-Yun Chou:** Validation. **Yu-Xen Lin:** Software. **Wanchai Assavalapsakul:** Supervision. **Arunee Thitithanyanont:** Supervision. **Li-Chen Su:** Writing – original draft, Writing – review & editing, Supervision, Funding acquisition, Project administration.

Declaration of Competing Interest

The authors declare that they have no known competing financial interests or personal relationships that could have appeared to influence the work reported in this paper.

Data availability

The authors confirm that the data supporting the findings of this study are available within the article and its supplementary materials.

Acknowledgments

This work was supported by grants from the National Science and Technology Council, Taiwan, under Grant 111-2112-M-131-005, 108-2320-B-037-035-MY3, 112-2320-B-037-032-MY3 and 112-2628-E-131-001-MY4, and Kaohsiung Medical University Research Center Grant (KMU-TC112B01), a grant from the Kaohsiung Medical University Research Foundation (KMU-M108006 & KMU-M112007) as well as a grant from Kaohsiung Medical University (KMU-DK(B)111002-5). Chang Gung Memorial Hospital, Linkou, Taiwan (CMRPD2M0042). The authors gratefully acknowledge Dr. Sheng-Wei Lin of Technology Commons, College of Life Science, National Taiwan University, Taiwan who provided us with a lot of helpful information and assistance about Biacore T200™.

Author contributions

All authors have given approval to the final version of the manuscript.

Supporting information

Presentation of noise current and detectivities for the corresponding OPDs with distinct thicknesses of the active layer; LDRs of the OPDs, each fabricated with distinct active layer thicknesses, illuminated by a 980 nm light source under a 0 V bias; Performance characteristics of OPDs fabricated with distinct active layer thicknesses measured at 0 V Bias.

Appendix A. Supporting information

Supplementary data associated with this article can be found in the online version at doi:10.1016/j.snb.2023.134898.

References

[1] H. Chen, G.J.D. Smith, K.S. Li, J. Wang, X.H. Fan, J.M. Rayner, et al., Establishment of multiple sublineages of H5N1 influenza virus in Asia: implications for pandemic control, Proc. Natl. Acad. Sci. 103 (2006) 2845–2850.
[2] K.S. Li, Y. Guan, J. Wang, G.J.D. Smith, K.M. Xu, L. Duan, et al., Genesis of a highly pathogenic and potentially pandemic H5N1 influenza virus in eastern Asia, Nature 430 (2004) 209–213.

[3] G. Neumann, H. Chen, G.F. Gao, Y.L. Shu, Y. Kawaoka, H5N1 influenza viruses: outbreaks and biological properties, Cell Res. 20 (2010) 51–61.
[4] ⟨https://www.who.int/news/item/12–07-2023-ongoing-avian-influenza-outbreaks-in-animals-pose-risk-to-humans⟩.
[5] J.X. Hou, X.J. Qian, Y. Xu, Z.R. Guo, B. Thierry, C.T. Yang, et al., Rapid and reliable ultrasensitive detection of pathogenic H9N2 viruses through virus-binding phage nanofibers decorated with gold nanoparticles, Biosens. Bioelectron. 237 (2023), 115423.
[6] C.M. Das, F. Yang, Z.X. Yang, X.C. Liu, Q.T. Hoang, Z.J. Xu, et al., Computational modeling for intelligent surface plasmon resonance sensor design and experimental schemes for real-time plasmonic biosensing: a review, Adv. Theory Simul. (2023) (Early Access).
[7] A. Azzouz, L. Hejji, K.H. Kim, D. Kukkar, B. Souhail, N. Bhardwaj, et al., Advances in surface plasmon resonance-based biosensor technologies for cancer biomarker detection, Biosens. Bioelectron. 197 (2022), 113767.
[8] J.J. Xue, Y.X. Zhang, W. Liu, Y. Zhang, S. Li, Z.H. Liu, et al., Ultrahigh-sensitivity SPR fiber temperature sensor based Ge(2)Sb(2)Te(5)and cyclohexane, Sens. Actuator A: Phys. 345 (2022), 113786.
[9] S.M. Chen, Y. Liu, Q.X. Yu, W. Peng, Self-referencing SPR biosensing with an ultralow limit-of-detection using long-wavelength excitation, Sens. Actuator B: Chem. 327 (2021), 128935.
[10] S.M. Chen, S.W. Chu, Y.X. Song, H.J. Wu, Y. Liu, W. Peng, Near-infrared surface plasmon resonance sensor with a graphene-gold surface architecture for ultra-sensitive biodetection, Anal. Chim. Acta 1205 (2022), 339692.
[11] F.C. Chien, S.J. Chen, A sensitivity comparison of optical biosensors based on four different surface plasmon resonance modes, Biosens. Bioelectron. 20 (2004) 633–642.
[12] J. Homola, On the sensitivity of surface plasmon resonance sensors with spectral interrogation, Sens. Actuator B: Chem. 41 (1997) 207–211.
[13] B.P. Nelson, A.G. Frutos, J.M. Brockman, R.M. Corn, Near-infrared surface plasmon resonance measurements of ultrathin films. 1. Angle shift and SPR imaging experiments, Anal. Chem. 71 (1999) 3928–3934.
[14] C. Lertvachirapaiboon, A. Baba, K. Shinbo, K. Kato, A smartphone-based surface plasmon resonance platform, Anal. Methods 10 (2018) 4732–4740.
[15] C. Xiao, G. Ross, M.W.F. Nielen, J. Eriksson, G.I. Salentijn, W.C. Mak, A portable smartphone-based imaging surface plasmon resonance biosensor for allergen detection in plant-based milks, Talanta 257 (2023), 124366.
[16] J.F. Masson, Portable and field-deployed surface plasmon resonance and plasmonic sensors, Analyst 145 (2020) 3776–3800.
[17] S. Priya, R. Laha, V.R. Dantham, Wavelength-dependent angular shift and figure of merit of silver-based surface plasmon resonance biosensor, Sens. Actuator A: Phys. 315 (2020), 112289.
[18] K.J. Ma, L. Liu, P.F. Zhang, Y.H. He, Q. Peng, Optimization of angle-pixel resolution for angular plasmonic biosensors, Sens. Actuator B: Chem. 283 (2019) 188–197.
[19] K. Thadson, S. Sasivimolkul, P. Suvarnaphaet, S. Visitsattapongse, S. Pechprasarn, Measurement precision enhancement of surface plasmon resonance based angular scanning detection using deep learning, Sci. Rep. 12 (2022) 2052.
[20] Z.C. Huo, Y. Li, B. Chen, W.C. Zhang, X.C. Yang, X.A. Yang, Recent advances in surface plasmon resonance imaging and biological applications, Talanta 255 (2023), 124213.
[21] R. Kashyap, A. Bhattacharjee, K. Rangpi, N.H. Barbhuiya, B. Mondal, Portable surface plasmon resonance (SPR) measurement device for sensing applications, 2020 IEEE 17th India Council International Conference (INDICON)2020, pp. 1–5.
[22] X.L. Wang, Y.J. Zeng, J. Zhou, J.J. Chen, R.B. Miyan, H. Zhang, et al., Ultrafast surface plasmon resonance imaging sensor via the high-precision four-parameter-based spectral curve readjusting method, Anal. Chem. 93 (2021) 828–833.
[23] H. Sipova-Jungova, L. Jurgova, E. Hemmerova, J. Homola, Interaction of Tris with DNA molecules and carboxylic groups on self-assembled monolayers of alkanethiols measured with surface plasmon resonance, Appl. Surf. Sci. 546 (2021), 148984.
[24] L.C. Chen, M.C. Li, K.R. Chen, Y.J. Cheng, X.Y. Wu, S.A. Chen, et al., Facile and unplugged surface plasmon resonance biosensor with NIR-emitting perovskite nanocomposites for fast detection of SARS-CoV-2, Anal. Chem. 95 (2023) 7186–7194.
[25] N. Vashistha, M.J. Abuleil, A.M. Shrivastav, A. Bajaj, I. Abdulhalim, Real-time ellipsometric surface plasmon resonance sensor using polarization camera may provide the ultimate detection limit, Biosensors 13 (2023) 173.
[26] M. Kashif, M.H.H. Mokhtar, N.H. Azeman, F.H. Hashim, N. Arsad, A.A. G. Abushagur, et al., Phase-interrogated surface plasmon resonance sensor based on laser feedback interferometry, Opt. Lasers Eng. 141 (2021), 106564.
[27] M.C. Li, K.R. Chen, C.C. Kuo, Y.X. Lin, L.C. Su, A simple phase-sensitive surface plasmon resonance sensor based on simultaneous polarization measurement strategy, Sensors 21 (2021) 7615.
[28] Y.F. Chang, Y.T. Chou, C.Y. Cheng, J.F. Hsu, L.C. Su, J.A.A. Ho, Amplification-free detection of cytomegalovirus miRNA using a modification-free surface plasmon resonance biosensor, Anal. Chem. 93 (2021) 8002–8009.
[29] Y.F. Chang, W.H. Wang, Y.W. Hong, R.Y. Yuan, K.H. Chen, Y.W. Huang, et al., Simple strategy for rapid and sensitive detection of avian influenza A H7N9 virus based on intensity-modulated spr biosensor and new generated antibody, Anal. Chem. 90 (2018) 1861–1869.
[30] R.K. Sinha, Wavelength modulation based surface plasmon resonance sensor for detection of cardiac marker proteins troponin I and troponin T, Sens. Actuator A: Phys. 332 (2021), 113104.
[31] Y.J. Zeng, J. Zhou, W. Sang, W.F. Kong, J.L. Qu, H.P. Ho, et al., High-sensitive surface plasmon resonance imaging biosensor based on dual-wavelength differential method, Front. Chem. 9 (2021), 801355.
[32] G. Simone, M.J. Dyson, S.C.J. Meskers, R.A.J. Janssen, G.H. Gelinck, Organic photodetectors and their application in large area and flexible image sensors: the role of dark current, Adv. Funct. Mater. 30 (2020) 1904205.
[33] J.F. Huang, J. Lee, J. Vollbrecht, V.V. Brus, A.L. Dixon, D.X. Cao, et al., A High-performance solution-processed organic photodetector for near-infrared sensing, Adv. Mater. 32 (2020) 1906027.
[34] Z.J. Zhao, C.Y. Xu, L.B. Niu, X.L. Zhang, F.J. Zhang, Recent progress on broadband organic photodetectors and their applications, Laser Photon Rev. 14 (2020) 2000262.
[35] P.C.Y. Chow, T. Someya, Organic photodetectors for next-generation wearable electronics, Adv. Mater. 32 (2020) 1902045.
[36] H. Ren, J.D. Chen, Y.Q. Li, J.X. Tang, Recent progress in organic photodetectors and their applications, Adv. Sci. 8 (2021) 2002418.
[37] N. Li, N. Eedugurala, J.D. Azoulay, T.N. Ng, A filterless organic photodetector electrically switchable between visible and infrared detection, Cell Rep. Phys. Sci. 3 (2022), 100711.
[38] Y.S. Lau, Z. Lan, L. Cai, F. Zhu, High-performance solution-processed large-area transparent self-powered organic near-infrared photodetectors, Mater. Today Energy 21 (2021), 100708.
[39] B.H. Jiang, F.C. Hsiao, Y.R. Lin, C.H. Lin, Y.A. Shen, Y.Y. Hsu, et al., Highly efficient ternary near-infrared organic photodetectors for biometric monitoring, ACS Appl. Mater. Interfaces (2023) (Early Access).
[40] Y.C. Huang, Z.H. Huang, T.Y. Wang, P. Chaudhary, J.F. Hsu, K.M. Lee, A promising non-fullerene acceptor for near-infrared organic photodetectors operating with low dark current and high response speed, Chem. Eng. J. 464 (2023), 142633.
[41] X.F. Liao, H.Q. Pei, H. Zhao, Y.J. Cui, L. Li, X.L. Shi, et al., The synergistic effects of central core size and end group engineering on performance of narrow bandgap nonfullerene acceptors, Chem. Eng. J. 435 (2022), 135020.
[42] W.T. Yang, W.M. Qu, E. Georgitzikis, E. Simoen, J. Serron, J. Lee, et al., Mitigating dark current for high-performance near-infrared organic photodiodes via charge blocking and defect passivation, ACS Appl. Mater. Interfaces 13 (2021) 16766–16774.
[43] Z.M. Zhong, L.J. Bu, P. Zhu, T. Xiao, B.B. Fan, L. Ying, et al., Dark current reduction strategy via a layer-by-layer solution process for a high-performance all-polymer photodetector, ACS Appl. Mater. Interfaces 11 (2019) 8350–8356.
[44] J.S. Liu, Y.X. Wang, H. Wen, Q.Y. Bao, L. Shen, L.M. Ding, Organic photodetectors: materials, structures, and challenges, Sol. RRL 4 (2020) 2000139.
[45] Y.M. Sung, A.K. Akbar, S. Biring, C.F. Li, Y.C. Huang, S.W. Liu, The effect of ZnO preparation on the performance of inverted polymer solar cells under one sun and indoor light, J. Mater. Chem. C 9 (2021) 1196.
[46] A. Sytchkova, A. Belosludtsev, L. Voloseviciene, R. Juskenas, R. Simniskis, Optical, structural and electrical properties of sputtered ultrathin chromium films, Opt. Mater. 121 (2021), 111530.
[47] D.I. Yakubovsky, A.V. Arsenin, Y.V. Stebunov, D.Y. Fedyanin, V.S. Volkov, Optical constants and structural properties of thin gold films, Opt. Express 25 (2017) 25574–25587.
[48] M.N. Hidayah, Z.N. Allaudin, P. Honari, O.P. Toung, M.-A. Mohd-Lila, Detection of classical swine fever virus by a surface plasmon resonance assay, Virol. Mycol. 3 (2014) 1000136.
[49] G.Z. Ma, R.L. Liang, Z.J. Wan, S.P. Wang, Critical angle reflection imaging for quantification of molecular interactions on glass surface, Nat. Commun. 12 (2021) 3365.
[50] C.Y. Lin, W.H. Wang, M.C. Li, Y.T. Lin, Z.S. Yang, A.N. Urbina, et al., Boosting the detection performance of severe acute respiratory syndrome coronavirus 2 test through a sensitive optical biosensor with new superior antibody, Bioeng. Transl. Med. (2022) (Early Access).
[51] S.F. Wang, K.H. Chen, A. Thitithanyanont, L. Yao, Y.M. Lee, Y.J. Chan, et al., Generating and characterizing monoclonal and polyclonal antibodies against avian H5N1 hemagglutinin protein, Biochem Biophys. Res. 382 (2009) 691–696.
[52] C.J. Shih, Y.C. Huang, T.Y. Wang, C.W. Yu, I.S. Hsu, A.K. Akbar, et al., Transparent organic upconversion devices displaying high-resolution, single-pixel, low-power infrared images perceived by human vision, Sci. Adv. 9 (2023) eadd7526.
[53] C.T. Yen, Y.C. Huang, Z.L. Yu, H.C. Cha, H.T. Hsiao, Y.T. Liang, et al., Performance improvement and characterization of spray-coated organic photodetectors, ACS Appl. Mater. Interfaces 10 (2018) 33399–33406.
[54] A.W. Peterson, M. Halter, A.L. Plant, J.T. Elliott, Surface plasmon resonance microscopy: achieving a quantitative optical response, Rev. Sci. Instrum. 87 (2016), 093703.
[55] M. Piliarik, J. Homola, Surface plasmon resonance (SPR) sensors: approaching their limits, Opt. Express 17 (2009) 16505–16517.
[56] P.H. Chung, P. Global Influenza, O. World Hlth, Expert consultation on diagnosis of H5N1 avian influenza infections in humans, Influenza Other Respir Viruses, 1 (2007), 131–138.
[57] S. Marche, T. van den Berg, Evaluation of rapid antigen detection kits for the diagnosis of highly pathogenic avian influenza H5N1 infection, Avian Dis. 54 (2010) 650–654.
[58] Y.J. Yang, Y.Y. Bai, Y.Y. Huangfu, X.Y. Yang, Y.S. Tian, Z.L. Zhang, Single-nanoparticle collision electrochemistry biosensor based on an electrocatalytic strategy for highly sensitive and specific detection of H7N9 avian influenza virus, Anal. Chem. 94 (2022) 8392–8398.
[59] F.W. Luo, C. Long, Z. Wu, H.Y. Xiong, M.M. Chen, X.H. Zhang, et al., Functional silica nanospheres for sensitive detection of H9N2 avian influenza virus based on immunomagnetic separation, Sens. Actuator B: Chem. 310 (2020), 127831.

[60] T. Matsubara, M. Ujie, T. Yamamoto, Y. Einaga, T. Daidoji, T. Nakaya, et al., Avian influenza virus detection by optimized peptide termination on a boron-doped diamond electrode, ACS Sens. 5 (2020) 431–439.
[61] I. Lee, S.E. Kim, J. Lee, D.H. Woo, S. Lee, H. Pyo, et al., A self-calibrating electrochemical aptasensing platform: correcting external interference errors for the reliable and stable detection of avian influenza viruses, Biosens. Bioelectron. 152 (2020), 112010.
[62] D. Kang, H.J. Ahn, J. Lee, S.K. Kim, J. Pyun, C.S. Song, et al., An NIR dual-emitting/absorbing inorganic compact pair: a self-calibrating LRET system for homogeneous virus detection, Biosens. Bioelectron. 190 (2021), 113369.
[63] J. Kwon, Y. Lee, T. Lee, J.H. Ahn, Aptamer-based field-effect transistor for detection of avian influenza virus in chicken serum, Anal. Chem. 92 (2020) 5524–5531.
[64] K. Nishiyama, Y. Takeda, M. Maeki, A. Ishida, H. Tani, K. Shigemura, et al., Rapid detection of anti-H5 avian influenza virus antibody by fluorescence polarization immunoassay using a portable fluorescence polarization analyzer, Sens. Actuator B: Chem. 316 (2020), 128160.
[65] D.G. Jiang, Y.F. Tian, Y.J. Zhang, X.Y. Lu, D. Xiao, C.S. Zhou, One-step fast and label-free imaging array for multiplexed detection of trace avian influenza viruses, Anal. Chim. Acta 1171 (2021), 338645.
[66] H. Jung, S.H. Park, J. Lee, B. Lee, J. Park, Y. Seok, et al., A size-selectively biomolecule-immobilized nanoprobe-based chemiluminescent lateral flow immunoassay for detection of avian-origin viruses, Anal. Chem. 93 (2021) 792–800.

Yu-Ching Huang is currently an Associate Professor in the Department of Materials Engineering at Ming Chi University of Technology, Taiwan. He received his PhD degree in the Institute of Materials Science and Engineering of National Taiwan University. His research interests are in printing flexible organic electronics and dim-light photovoltaics applications.

Sheng-Fan Wang is currently a Professor in the Department of laboratory Science and Biotechnology at Kaohsiung Medical University, Taiwan. He received his PhD degree in the Department of Biotechnology and Laboratory Science in Medicine of National Yang-Ming University. His research interest fields mainly focus on virology, immunology and emerging infectious disease.

Bo-Cheng Chen is now a master student in the Department of Materials Engineering at Ming Chi University of Technology, Taiwan.

Zih-Syuan Yang is now a PhD student in the Department of laboratory Science and Biotechnology at Kaohsiung Medical University, Taiwan.

Meng-Chi Li is currently an Assistant Professor in the General Education Center at Ming Chi University of Technology, Taiwan. He received his PhD degree in the Department of Optics and Photonics of National Central University. His research mainly focuses on thin-film optics and optical testing.

Xun-Ying Wu is now a master student in the Department of Mechanical Engineering at Ming Chi University of Technology, Taiwan.

Meng-Jey Youh is currently a Professor in the Department of Mechanical Engineering at Ming Chi University of Technology, Taiwan. He received his PhD degree in the School of Physics at Bristol University. His research interests are in field emission component development and computer embedded system development.

Hui-Yun Chou is now a master student in the Department of Mechanical Engineering at Ming Chi University of Technology, Taiwan.

Yu-Xen Lin is received hid MS degree in the Department of Optics and Photonics at National Central University, Taiwan. His main interests are in software development.

Wanchai Assavalapsakul is currently an Associate Professor in the Department of Microbiology at Chulalongkorn University. He received his PhD degree in the Institute of Molecular Biosciences of Mahidol University. His research interests are in diagnostic and vaccine development for viral disease in livestock.

Arunee Thitithanyanont is currently an Associate Professor in the Department of Microbiology at Mahidol University. Her research interests are in Emerging viruses and pandemic preparedness innovations.

Li-Chen Su is currently an Associate Professor in the General Education Center at Ming Chi University of Technology, Taiwan. She received her PhD degree in the Department of Optics and Photonics of National Central University. Her research interests are in the development and application of nanotechnology-based optical biosensors.